Structural phase transition, optical and electrical properties of the hybrid material [(C2H5)4N]2ZnI4

H. Elgahami, J. Lhoste, S. Auguste, Gwenaël Corbel, A. Oueslati

Structural phase transition, optical and electrical properties of the hybrid material $[(C_2H_5)_4N]_2ZnI_4$

H. Elgahami [1,*], J. Lhoste [2], S. Auguste [2], G. Corbel [2] and A. Oueslati [1]

[1] *Laboratory for Spectroscopic Characterization and Optics of Materials, Faculty of Sciences, University of Sfax, B. P. 1171, 3000, Sfax, Tunisia*
[2] *Institut des Molécules et Matériaux du Mans (IMMM), UMR-6283 CNRS, Le Mans Université, Avenue Olivier Messiaen, 72085 Le Mans Cedex 9, France*
** E-mail: hanengahami1993@gmail.com*

Abstract

The bis (tetra-ethylammonium) tetraiodo-zincate (II) was prepared by slow evaporation an aqueous stoichiometric mixture of tetra-ethylammonium iodide and zinc iodide at room temperature. This compound has been characterized by X-ray diffraction (XRD), thermal analysis, UV–vis spectroscopy and complex impedance spectroscopy. Single crystal X-ray diffraction analysis shows that the title compound crystallizes in the tetragonal system with space group P 42_1m.The differential thermal analysis (DTA) and temperature-controlled X-ray diffraction study reveal a reversible first order phase transition at about 444 K between low temperature-tetragonal and high temperature-orthorhombic forms of $[(C_2H_5)_4N]_2ZnI_4$. Below 444 K, the low temperature form exhibits two linear regimes of thermal expansion with a change in the slope around 373 K which is ascribed to a second-order phase transition. The diffuse reflectance indicates the existence of an optical direct transition with the band gap energy is equal to 3.9 eV. The spectra of complex impedances obtained in the temperature range from 403 to 468 K were modelled by a combination of R//CPE elements. A change of conduction regime around 444 K is noted in the variation of the Ln (σ_{DC}.T) versus reciprocal temperature. In both regimes, the conductivity obeys the Arrhenius law with activation energies of 1.37 eV in regime I and 2.37 eV in regime II. Frequency dependence of the AC conductivity followed the universal Jonscher's power law.

1-Introduction

The prospect of creating new functional materials with tunable properties gives a strong motivation to research on organic-inorganic compounds [1]. The increasing interest is based not only on their structural variety but also on their uses in many applications such as electronics (as thin film transistor, Organic-Inorganic Emitting Diode) and data storage to photovoltaic devices [2–5]. The introduction of hybrid materials in solar cells was represented a field breakthrough, allowing novel device architectures leading to record enhanced performances [6,7]. In this aim, the halogenometallates of a general formula $[A]_2MX_4$ (A = organic cation, M = metal ion, X = Cl, Br, or I anion) constitute a large family of compounds with different crystal structures depending on the size of the organic cation A and which exhibit phase transitions upon heating [8–15]. Furthermore, the series of tetra-methyl ammonium compounds $[(CH_3)_4N]_2MX_4$ (M = Zn, Co, Ni, Fe, Cu, Hg, X = Cl, Br) show various phase transitions such as the ferroelectric or ferroelastic transitions [16–20]. Structural phase transitions were also detected in several tetra-ethylammonium compounds $[(C_2H_5)_4N]_2MeX_4$ (M = Zn, Co, Ni, Fe, Cu, Hg, X = Cl, Br) [21–25].

The iodometallates are principally of interest in comparison with the bromometallates and chlorometallates as they tend to possess smaller band gaps and lower carrier effective masses which are important properties for high performance optoelectronic materials [26,27].

Harrison et al. isolated single crystals of $[(C_2H_5)_4N]_2ZnI_4$ from the reaction in ethanol of bis(tetraethylammonium) $Zn(DMIT)_2$ (where DMIT is the dianion of 1,3-dithiole-2-thione-4,5-dithiol) with a source of iodide (SbI_3 or AsI_3) [28]. Unfortunately, this synthetic route does not allow $[(C_2H_5)_4N]_2ZnI_4$ to be obtained as the only phase, since another reaction product containing trivalent antimony or arsenic cations and DMIT anions is inevitably present. In order to study the phase transitions and physical properties of $[(C_2H_5)_4N]_2ZnI_4$, a large amount of crystals exempt of any secondary phase is necessary. Our previous studies show that crystal growth of pure organic-inorganic halides occurs by slowly evaporating a solution of alkylammonium halide and metal halide at room temperature. Recently, we were able to synthesize by this method a large amount of $[(C_2H_5)_4N]_2ZnI_4$ crystals, thus allowing, for the first time, to investigate its thermal behaviour by a combination of

thermogravimetric analysis (DTA and TAG) and temperature-controlled X-ray powder diffraction and to measure its optical and electrical properties by means of UV–visible and complex impedance spectroscopies. To check that the crystals correspond to $[(C_2H_5)_4N]_2ZnI_4$, the structure was re-determined at room temperature and compared with that of Harrison et al. before any investigation.

2-Experimental

In this paper, the $[(C_2H_5)_4N]_2ZnI_4$ crystals were obtained by slow evaporation at room temperature from a stoichiometric quantities of tetraethylammonium iodide $[(C_2H_5)_4N]I$ (98%, Aldrich) and zinc iodide (ZnI_2) dissolved in distilled water. Colorless crystals of millimeter size grew in few days and then characterized by different techniques. To check that the crystals correspond to the title compound, their structure was re-determined at room temperature and compared with that of Harrison et al.

The corresponding chemical reaction is:

$$2\left[(C_2H_5)_4N\right]I + ZnI_2 \xrightarrow{H_2O} C_2H_5)(C_2H_5)(C_2H_5)_4N]_2ZnI_4$$

A suitable crystal for X-ray diffraction was selected by an optical examination and mounted on MicroMount needles. X-ray intensity data were collected on a Bruker APEX II Quazar diffractometer (4 circle Kappa goniometer, CCD detector) using microfocus source (Mo-Kα radiation with λ = 0.71073 Å) at 296 K. Absorption correction was performed by multi-scan method implemented in SADABS [29].The structure solutions were obtained by direct methods, developed by successive difference Fourier syntheses and refined by full-matrix least-squares on all $|F|^2$ data using SHELX program [30] suite in WinGX interface [31]. Crystal structure has been solved in the tetragonal system with non-centrosymmetric space group $P\,\overline{4}\,2_1m$ (No.113). All non-hydrogen atoms positions have been refined anisotropically whereas hydrogen atoms of the amine molecules have been geometrically constrained (HFIX options). We note that no hydrogen atom could be placed on an independent organic molecule due to the partial occupation of C atoms. A summary of the key crystallographic data is summarized in Table 1. The fractional atomic coordinates and equivalent isotropic displacement parameters (Å^2) are given in Table 2. Selected bond lengths and angles are listed in Table 3. Since the structural model we obtained is identical to that found by Harrison et al., we were able to study the thermal behaviour of this compound and measure its electrical conductivity.

Atomic coordinates, anisotropic displacement parameters, tables for all bond distances and angles have been deposited at the Cambridge Crystallographic Data Centre (deposition number: CCDC 2075309).

Thermogravimetric and differential thermal analyses were

Table 1
Parameters of data collection, and results of structure refinement for $[(C_2H_5)_4N]_2ZnI_4$.

Crystal data	
Chemical formula	$C_{16}H_{40}N_2$ Zn I_4
Molecular weight (g.mol^{-1})	871.45
Crystal system, space group	Tetragonal, P42$_1$m
Temperature (K)	296
a, *c* (Å)	13.7947(2), 14.9001 (3)
V (Å^3)	2835.40 (1)
Z	4
Radiation type	Mo K_α
μ (mm^{-1})	5.23
No. of measured, independent and observed [$I > 2\sigma(I)$] reflections	77772, 3469, 2682
R_{int}	0.058
D_{cal} (Mg m^{-3})	2.041
$R[\|F^2\| > 2\sigma(\|F^2\|)]$, $wR(\|F^2\|)$, *S*	0.036, 0.116, 1.04
No. of reflections	3469
No. of parameters	134
$\Delta\rho_{max}$, $\Delta\rho_{min}$ (e Å^{-3})	0.83, −0.94
θ range for data collection (°)	1.4–27.5
Absolute structure parameter	0.020 (2)
Range of h k l	h = −17 → 17 k = −17 → 17 l = −19 → 19

Table 2
Fractional atomic coordinates, site occupancy (%) and equivalent isotropic displacement parameters (Å^2).

Atom	*X*	*Y*	*z*	U_{iso}*/U_{eq}	Occ.(<1)
I1	0.75505 (7)	1.25505 (7)	0.94638 (6)	0.0747 (3)	
I2	0.79538 (8)	1.07357 (6)	0.71917 (6)	0.0941 (3)	
I3	0.87003 (7)	1.37003 (7)	0.70150 (9)	0.0893 (4)	
Zn1	0.74777 (9)	1.24777 (9)	0.77105 (10)	0.0589 (4)	
N1	0.0000	1.0000	0.0000	0.054 (4)	
C2	−0.1159 (10)	1.0495 (13)	0.1269 (9)	0.093 (4)	
H2A	−0.1605	1.0052	0.0993	0.140*	
H2B	−0.1504	1.1058	0.1473	0.140*	
H2C	−0.0851	1.0185	0.1771	0.140*	
C1	−0.0368 (11)	1.0807 (11)	0.0567 (10)	0.087 (4)	
H1A	−0.0640	1.1302	0.0179	0.105*	
H1B	0.0174	1.1094	0.0885	0.105*	
N2	0.7909 (7)	0.7091 (7)	0.5808 (9)	0.069 (3)	
C3	0.7168 (12)	0.7832 (12)	0.5489 (19)	0.114 (8)	
H3A	0.7505	0.8294	0.5111	0.137*	0.5
H3B	0.6706	0.7495	0.5111	0.137*	0.5
C4	0.6600 (16)	0.8400 (16)	0.617 (3)	0.18 (2)	
H4A	0.6616	0.9075	0.6010	0.275*	0.5
H4B	0.6880	0.8311	0.6750	0.275*	0.5
H4C	0.5941	0.8177	0.6170	0.275*	0.5
C5	0.7456 (15)	0.6348 (14)	0.6351 (10)	0.117 (6)	
H5A	0.7169	0.6647	0.6877	0.141*	
H5B	0.7949	0.5897	0.6555	0.141*	
C6	0.6643 (15)	0.5765 (15)	0.5827 (16)	0.138 (8)	
H6A	0.6075	0.6162	0.5767	0.207*	
H6B	0.6483	0.5187	0.6154	0.207*	
H6C	0.6878	0.5593	0.5242	0.207*	
C7	0.8346 (15)	0.6654 (15)	0.4977 (14)	0.114 (9)	
H7A	0.7826	0.6373	0.4625	0.136*	0.5
H7B	0.8627	0.7174	0.4625	0.136*	0.5
C8	0.9078 (13)	0.5922 (13)	0.510 (2)	0.141 (12)	
H8A	0.9033	0.5451	0.4629	0.212*	0.5
H8B	0.8983	0.5608	0.5670	0.212*	0.5
H8C	0.9708	0.6218	0.5090	0.212*	0.5
N3	0.5000	1.0000	−0.0183 (16)	0.079 (6)	
C9	0.486 (2)	0.909 (2)	0.041 (2)	0.098 (8)	0.5
C10	0.4102 (12)	0.9102 (12)	0.1114 (17)	0.110 (8)	
C12	0.409 (2)	0.091 (2)	0.856 (2)	0.194 (19)	
C11	0.487 (3)	0.091 (3)	0.927 (3)	0.136 (15)	0.5

Table 3
Selected bond lengths d (Å) and bond angles ω (deg) for $[(C_2H_5)_4N]_2ZnI_4$.

Lengths	d (Å)	Angles	ω (°)
I1–Zn1	2.616 (2)	I3–Zn1–I2	108.43 (5)
I2^{i}—Zn1	2.608 (1)	I3–Zn1–I1	110.37 (7)
I3–Zn1	2.601 (2)	I2–Zn1–I1	108.76 (5)
N1–C1^{ii}	1.486 (1)	C1^{ii}—N1—C1^{iv}	108.8 (6)
C2–C1^{iii}	1.57 (2)	N1–C1–C2	114.2 (1)
N2–C5^{v}	0.960	C5^{v}—N2—C7	110.5 (1)
N2–C7	0.960	C5^{v}—N2—C3	111.1 (1)
N2–C3	0.970	C7–N2–C3	106.4 (2)
C3–C4	0.970	C4–C3–N2	120 (2)
C5–C6	1.448 (2)	N2–C5–C6	112.9 (1)
C7–C8	1.440 (4)	C8–C7–N2	117 (2)
N3–C11^{vi}	1.51 (3)	C11^{vii}—N3—C11^{vii}	114 (4)
N3–C9^{v}	1.54 (3)	C11^{vii}—N3—C9^{v}	109 (2)
C9–C10	1.48 (4)	C10– C9–N3	119 (2)
C9–C11^{vii}	1.75 (5)	C10–C9–C11^{vii}	147 (3)
C12–C11	1.51 (4)	N3–C9–C11^{vii}	54.1 (2)
		C12–C11–N3	118 (3)
		C12–C11–C9	147 (4)

Symmetry codes: (i) y-1/2, x++1/2, z; (ii) –y+1, x+1, -z; (iii) y-1, -x+1, -z; (iv) –x, -y+2, z; (v) -y+3/2, -x+3/2, z; (vi) –y+1/2, -x+3/2, z-1; (vii) –x+1,-y+1, z-1.

simultaneously performed on crushed crystals of $[(C_2H_5)_4N]_2ZnI_4$with a TGA/DTA Q600 SDT TA Instruments apparatus (Pt crucibles, α-Al_2O_3 as a reference) under air flow (100 mL/min) from the room temperature (RT) to 473 K range (heating/cooling rate of 5 °C/min).

The phase purity of the powder was checked by recording X-ray powder diffraction (XRPD) pattern at room temperature on a PANalyticalθ/θ Bragg-Brentano Empyrean diffractometer ($CuK_{\alpha 1+2}$ radiations) equipped with the PIXcel^{1D} detector. XRPD pattern was collected at room temperature in the [5°–65°] scattering angle range, with a 0.0131° step size, for a total acquisition time of 5 h 30 min. Thermal stability in air of the as-prepared powder was studied by temperature-controlled X-ray powder diffraction. XRPD patterns were recorded on the same diffractometer between 298 and 473 K (heating rate of 2 K/min, temperature stabilisation for 20 min, cooling rate of 60 K/min, air flow of 40 mL/min) by using an XRK 900 Anton Paar reactor chamber. The sample was deposited on the sieve (pore size Æ 0.2 mm) of the open sample holder cup, both made of glass ceramic Macor®, thus allowing air to flow through the sample. For each temperature, the XRPD pattern was collected in the [5°–44°] scattering angle range, with a 0.0131° step size, for a total acquisition time of 2 h. The refinements of the XRPD pattern were carried out by the Le Bail method [32] of the Fullprof program [33].

Optical properties were carried out by means of a UV-VIS spectrophotometer (UV–vis Scanning Spectrophotometer (UV-3101PC)) in the wavelength range of 200–800 nm.

The powder was shaped into a cylindrical pellet of 8 mm diameter and 1.1 mm thickness. The electrical measurements were measured in the frequency ranging from 100 Hz to 5 MHz using a 1260 Solartron Impedance Analyzer. To obtain the good electrical contact, the pellet is covered on the opposite surfaces with thin layer of Ag and was mounted between two copper electrodes in a special holder. Measurements were carried out as a function of temperatures in the range 403–468 K.

3-Results of experimental measurements and discussion

3-1) Crystal structure at RT

The asymmetric unit of $[(C_2H_5)_4N]_2ZnI_4$ reveals that the crystal structure is built by two tetraethylammonium cations $[(C_2H_5)_4N]^+$ and one tetra-iodozincate anion $[ZnI_4]^{2-}$ (Fig. 1). Along the c axis, the structural arrangement consists of tetrahedral $[ZnI_4]^{2-}$ surrounded by tetraethylammonium (TEA) cations (Fig. 2).

Three types of TEA cations can be recognized in the structure, two of which in a "swastika" conformation (one ordered, one disordered) and a third one in a virtually planar trans conformation. There are several structures reported in the literature, in which the TEA group adopts one of these two stable conformations. The trans conformation, found in

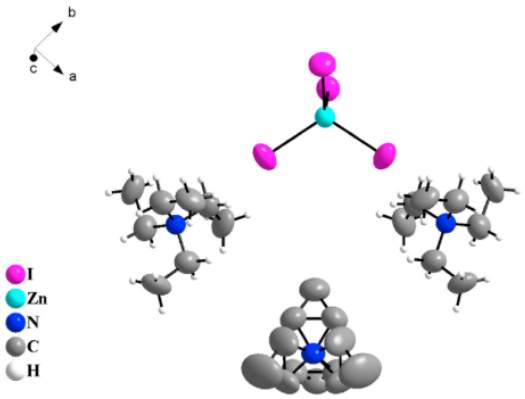

Fig. 1. Asymmetric unit of $[(C_2H_5)_4N]_2ZnI_4$.

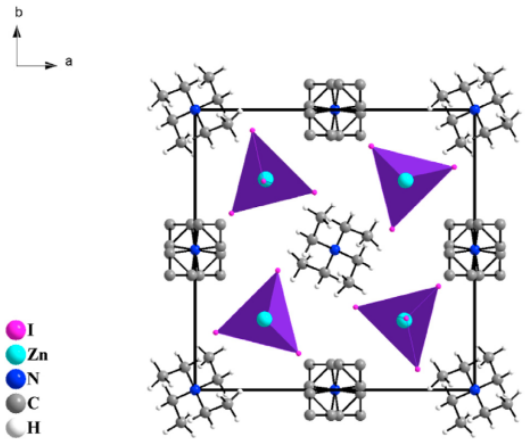

Fig. 2. Projection in the plane (ab) of the atomic arrangement of $[(C_2H_5)_4N]_2ZnI_4$.

several compounds such as $[(C_2H_5)_4N]SbBr_6$ [34],$[(C_2H_5)_4N]AuCl_2$ [35] and$[(C_2H_5)_4N]_2InCl_5$ [36]. The "swastika" arrangement is more common and is usually encountered in the $[(C_2H_5)_4N]_2MX_4$ family such as $[(C_2H_5)_4N]_2NiCl_4$, $[(C_2H_5)_4N]_2CoCl_4$ [37], $[(C_2H_5)_4N]NiBr_4$ [38], $[(C_2H_5)_4N]_2HgCl_4$ [39], $[(C_2H_5)_4N]_2CdCl_4$ [40], $[(C_2H_5)_4N]_2ZnCl_4$ [41] but also in other compounds like $[(C_2H_5)_4N]CuCl_4{\cdot}5H_2O$ [42], $[(C_2H_5)_4N]Pt_2Br_5$ [43]. In some of these structures, the TEA groups show a disorder similar to that observed in the present compound.

The cohesion between the $[(C_2H_5)_4N]^+$ and $[ZnI_4]^{2-}$ ions are ensured by electrostatic interactions and hydrogen bonds of C–H ····I type (Fig. 3). The length and angles of defining these hydrogen bonds are listed in Table 4.

A part of the crystals thus formed have been crushed in order to check the sample homogeneity by recording X-ray powder diffraction (XRPD) pattern at room temperature. A refinement of the XRPD pattern collected at room temperature was carried out by the Le Bail method using the tetragonal system and the $P\bar{4}2_1m$ (No.113) space group determined from the single crystal X-ray diffraction study. Fig. 4 shows the observed, calculated and difference diffraction patterns for $[(C_2H_5)_4N]_2ZnI_4$. All Bragg peaks were successfully indexed and satisfactorily modelled, thus confirming the high purity of the sample. The conventional reliability factors of the refinement are $R_p = 7.42\%$, $R_{\omega p} = 7.42\%$, $R_{exp} = 2.15\%$.

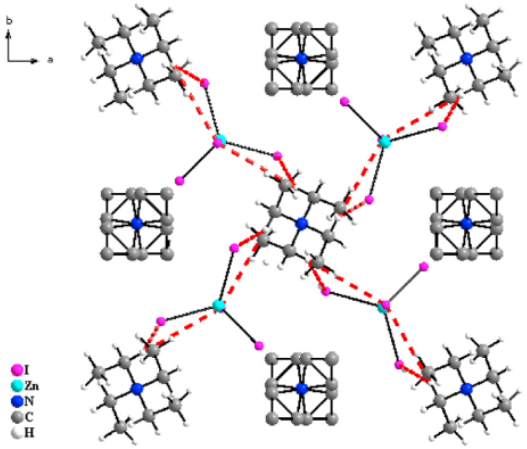

Fig. 3. Intermolecular hydrogen bonds of $[(C_2H_5)_4N]_2ZnI_4$compound.

Table 4
Principal interatomic distances (Å) and bond angles (°) of the hydrogen bonding.

D-H	d(D-H)	d(H … A)	D-H … A	d(D … A)	A
C1-H1A	0.970	3.215	151.05	4.091	I1
C1-H1B	0.970	3.246	141.38	4.049	I2
C4-H4C	0.970	3.178	148.19	4.026	I2
C5-H5B	0.970	3.276	151.65	4.155	I3
C7-H7A	0.970	3.042	149.18	3.907	I2
C7-H7B	0.970	3.042	149.18	3.907	I2

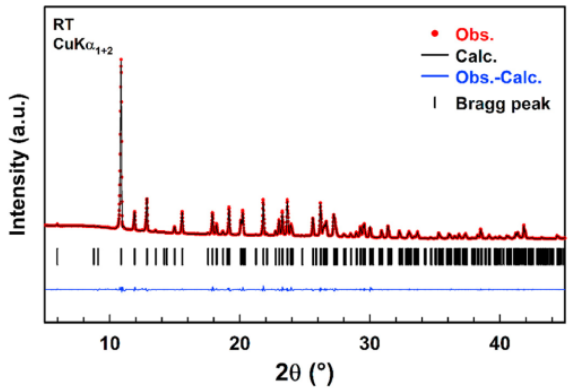

Fig. 4. Comparison of the observed diffraction pattern collected on the $[(C_2H_5)_4N]_2ZnI_4$ powder (red dots) with the pattern calculated by the Bail method (black line). The blue curve corresponds to the difference between observed and calculated patterns. Vertical markers give Bragg peak positions (space group $\bar{P}\,42_1m$ (No.113)).

The tetragonal cell parameters, a = 13.8010(5) Å and c = 14.8999(7) Å are in good agreement with those determined from XRD data collected on a single crystal.

3-2) Thermal analysis

The thermal stability of crushed crystals of the title compound was studied in the temperature range RT- 473 K by means of simultaneous thermogravimetric and differential thermal analyses (TGA-DTA). In Fig. 5a one endothermic and one exothermic peaks are observed in the DTA curve at 444 K on heating up and at 420 K on cooling down the powder at 5 K/min, respectively. No weight loss is measured in the whole temperature range RT-473 K (Fig. 5a). An XRPD pattern was collected on the $[(C_2H_5)_4N]_2ZnI_4$ powder after the thermal analysis carried out up to 473 K and compared with that recorded before in Fig. 5b. As the XRPD pattern being identical before and after thermal analysis, no thermal decomposition of the sample occurs during heating to 473 K, which is also supported by the absence of weight loss during heating.This compound therefore exhibits a reversible structural phase transition of the first order at 444 K.

3-3) Temperature-controlled X-ray powder diffraction

Fig. 6 shows the thermal evolution of the XRPD patterns of $[(C_2H_5)_4N]_2ZnI_4$ in the range RT-473 K. The XRPD patterns collected above 438 K completely differs from those collected below this temperature. This change is attributed to the first order structural phase transition detected by DTA at 444 K. The determination of the crystal structure of an inorganic-organic compound from the Rietveld refinement of XRPD data is very challenging. For this reason, we did not attempt from the XRPD data to determine the crystal structure of the low and high temperature forms of $[(C_2H_5)_4N]_2ZnI_4$ existing below and

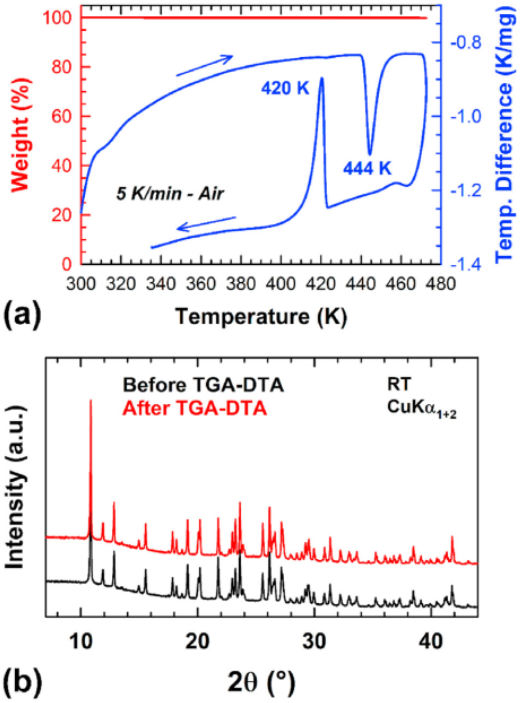

Fig. 5. (a) Thermogravimetric (red) and differential thermal (blue) curves recorded during heating and cooling of the $[(C_2H_5)_4N]_2ZnI_4$ powder in air. (b) XRPD patterns collected on the $[(C_2H_5)_4N]_2ZnI_4$powder before and after thermal analysis in air showing the reversible nature of the structural phase transition.

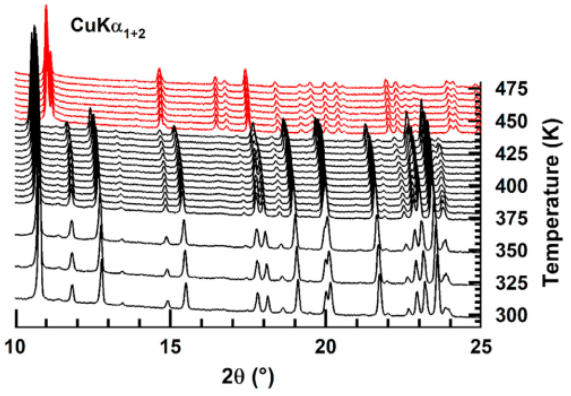

Fig. 6. XRPD patterns recorded during heating of the $[(C_2H_5)_4N]_2ZnI_4$ powder in air from RT to 473 K.

above 438 K, respectively. Only refinements of the XRPD patterns were carried out by the Le Bail method. For the refinement of the XRPD pattern collected at RT, the tetragonal cell parameters, we previously determined in section 3.1, were used as starting values. Successively, the cell parameters determined from the refinement of a lower temperature XRPD pattern was used as starting values for the refinement of the next higher temperature one. All XRPD patterns can be satisfactorily fitted in this way, thus confirming that the low temperature crystal structure of $[(C_2H_5)_4N]_2ZnI_4$ is preserved in the whole temperature range RT- 433 K.

The XRPD patterns collected at 443 K can be fully indexed with an orthorhombic unit cell (a ≈15.70 Å, b ≈ 18.00 Å and c ≈ 10.66 Å) and the space group *P na2₁* (No.33). All XRPD patterns collected in the temperature range 443–473 K were then successively refined by using this orthorhombic unit cell. The thermal evolutions of the cell parameters of both forms are displayed in Fig. 7. Surprisingly, two thermal domains with linear dependences are observed for each tetragonal cell parameter in the range RT-373 K and 373–433 K, respectively. The three orthorhombic cell parameters linearly increase with temperature in the range 443–473 K. From these linear evolutions, thermal expansion coefficients (TEC) along the different crystallographic axes are calculated for both forms and displayed in Table 5. Note that above 373 K, the TEC along the a axis increases while the TEC decreases along the *c* axis. Since no endothermic event is detected in the DTA curve at around 373 K (Fig. 5a), these changes in TECs can only be attributed to a structural phase transition of the second order. Such transition at 373 K could be due to small displacements/reorientations of the $[(C_2H_5)_4N]^+$ cations in the crystal structure.Whatever the crystallographic forms considered, the thermal expansion along the [001] direction is much smaller in magnitude than the one in the basal (*ab*) plane.

3-4) Optical properties

The optical properties of bis (tetra-ethylammonium) tetra-iodozincate (II) compound were evaluated by the UV–Vis absorption measured at room temperature. The experimental absorption spectrum of $[(C_2H_5)_4N]_2ZnI_4$ is plotted in Fig. 8. We observe the presence of seven distinct absorption peaks at 200, 237, 311, 367, 554, 581 and 618 nm, which are very similar to those found in other organic-inorganic hybrids materials, such as $[(C_2H_5)NH_3]_2ZnCl_4$ [44], $[C_7H_{16}N_2][ZnCl_4]$ [45] and $[(CH_3)NH_2]_2ZnCl_4$ [46].

The intense band observed around 200 nm is due to band gap absorption and it is assigned to the excitation of free electron hole pairs within the $[ZnCl_4]^{2-}$ inorganic anion. It is due mainly to the absorption between Cl (3p) and Zn (4s). Indeed, an electron is excited from the valence band (VB) permitted in the gap leaving a hole in the (VB). While, the other peaks at 237, 311, 367, 554, 581 and 618 nm can be attributed to the excitonic transition. The Kubelka-Munk method is used to analyze the reflectance of materials in the visible field.

The Kubelka-Munk function is expressed by the following equation: [47,48]:

$$F(R) = (1-R)^2/2R \quad (1)$$

where R is the reflectance of light.

The energy gap value can be determined by Tauc's expression [49]:

$$F(R).h\upsilon = B\ (h\upsilon - E_g)^n \quad (2)$$

where E_g is the energy gap, B is a constant and hν is the photonic energy expressed in eV, *n* takes two values depending on the nature of the transition allowed. Theoretically *n* is equal to 1/2 or 2 for a direct or indirect transition, respectively.

For this compound, n = 1/2 belongs to the direct band gap nature of the material. Because of the lattice phonons contribution in the direct allowed transitions (Fig. 9). The extrapolation of the linear region of the curve $(F(R)h\upsilon)^2$ versus hυ gives a value of 3.9 eV which indicates a semiconducting behaviour of the title compound [50–52].

3-5) Electrical properties

The Nyquist plots (-Z″ versus Z′) of $[(C_2H_5)_4N]_2ZnI_4$ compound collected at different temperatures are shown in Fig. 10. All impedance spectra show some dispersion and also the centers of the semicircles are on a line below the real axis, which confirms the Cole–Cole type of relaxation [53]. As the temperature increases, the radius of the semicircles observed and the associated resistance value progressively

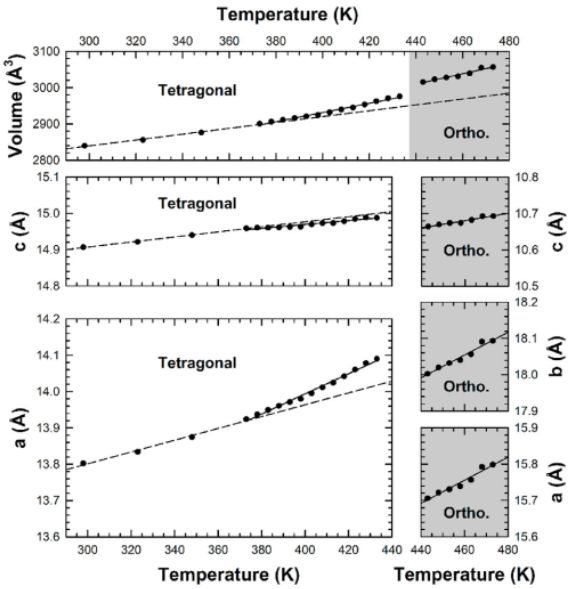

Fig. 7. Thermal evolutions of the cell parameters of the low temperature-tetragonaland high temperature-orthorhombic formsof the $[(C_2H_5)_4N]_2ZnI_4$ compound determined from the refinement by the Le Bail method of the XRPD patterns collected in the temperature range RT-473 K.

Table 5
Thermal Expansion Coefficients (TEC) of the low temperature-tetragonal and high temperature-orthorhombic forms of the $[(C_2H_5)_4N]_2ZnI_4$ compound.

	LT tetragonal form		HT orthorhombic form
	TEC (K^{-1}) RT- 373 K	TEC (K^{-1}) 373–433 K	TEC (K^{-1}) 443–473 K
a axis	1.62×10^{-3}	2.77×10^{-3}	3.18×10^{-3}
b axis			3.13×10^{-3}
c axis	6.96×10^{-4}	5.41×10^{-4}	1.00×10^{-3}

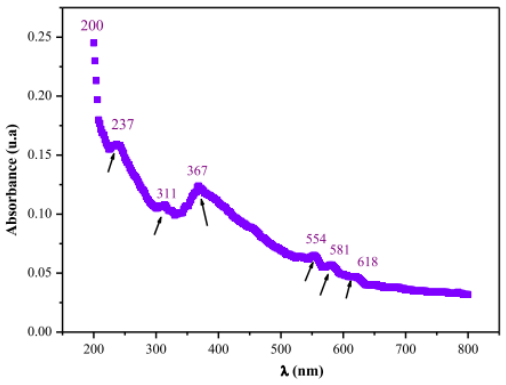

Fig. 8. UV–visible Absorption spectrum for $[(C_2H_5)_4N]_2ZnI_4$compound at room temperature.

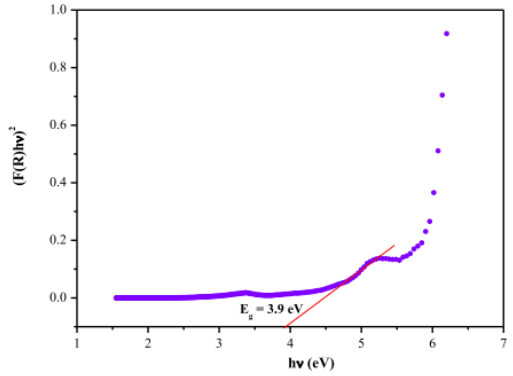

Fig. 9. Variation of the $(F(R)h\nu)^2$ vs $h\nu$.

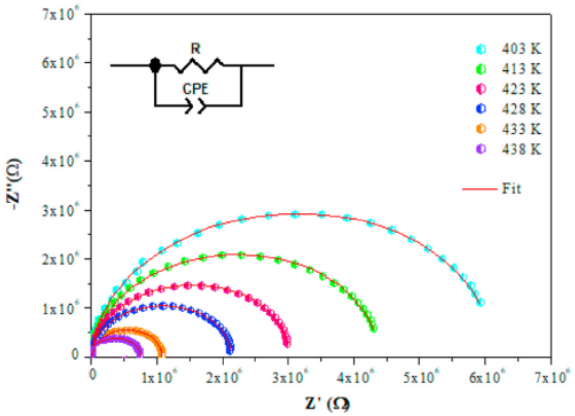

Fig. 10. Nyquist plots and fits of complex impedance spectra of $[(C_2H_5)_4N]_2ZnI_4$ recorded at different temperatures. The fits are performed with the electrical equivalent circuit given in insert.

decrease. So, the process of electrical conduction in the title compound is thermally activated [54].

Fits of spectra are performed by using Z-view software (solid line in Fig. 10) [55] by using an equivalent circuit formed by a parallel combination of a resistance R and a fractal capacity CPE. Based on the value of capacitance, this semicircle is assigned to the electrical response of grains [56]. Fig. 11 shows the variation of Z′ and -Z″ as a function of angular frequency at 413 K.

A good agreement between observed and calculated impedances is obtained by using the proposed equivalent circuit. It is clear that Z′ decreases with increasing frequency while -Z″ 'increases and reaches a maximum at a particular frequency where it intersects with Z′. From this frequency Z′ and -Z″ decrease and tend asymptotically towards the x-axis. This observation confirms the existence of a relaxation phenomenon [57, 58].

The temperature dependence of the DC-conductivity (Ln (σ_{DC}.T) versus (1000/T)) is shown in Fig. 12. At the first order phase transition (around 444 K) a change of slope is noted.

In both regions I (400–434 K) and II (444–465 K), the conductivity obeys a law of Arrhenius-type $\sigma_{DC}.T = A \exp(-E_a/k_B.T)$ where A is the pre-exponential factor, E_a is the activation energy and k_B is the Boltzmann constant. The activation energies obtained by a linear fit in regions

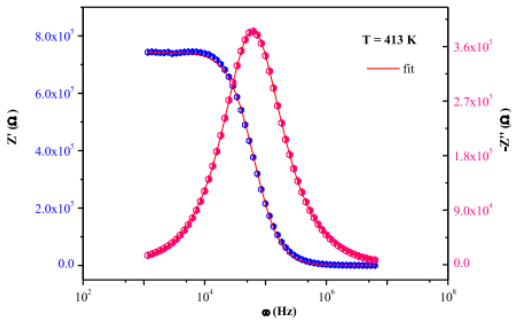

Fig. 11. Frequency dependence of Z′ and -Z″ at 413 K.

I and II are $E_{a1} = 1.37$ eV and $E_{a2} = 2.37$ eV, respectively.

The temperature dependence of the electrical conductivity (σ_{AC}) at different frequency can be defined by the Jonscher universal power law as [59]:

$$\sigma_{AC} = \sigma_{DC} + A\omega^S \quad (3)$$

where σ_{AC} is the conductivity in alternative current, σ_{DC} is the conductivity in continuous current, A is a constant, ω is the angular frequency ($\omega = 2\pi f$), S is an exponent expressing the degree of interaction between the mobile charge and its surrounding.

Fig. 13 shows the evolution of σ_{AC} as a function of the frequency. The conductivity pattern proves a typical behaviour of ionic material, that is it displayed a plateau-type response at low frequencies and at high frequencies, the conductivity indicates a dispersion pattern, which shifts toward higher frequency with increasing temperature, attributed to the AC conductivity. Whereas the frequency is independent of plateau at low frequencies, corresponds to DC conductivity of the material [60]. It is seen that the plateau region of the DC conductivity progressively extends towards the high frequencies as the temperature increases which indicates that the charge carriers can move easily at the high frequencies [61].

For each temperature the high and low frequency regions are separated by a change in slope at a certain value of frequency. This frequency is known as the hopping frequency [62].

The temperature dependence of the exponent S (Fig. 14) shows two

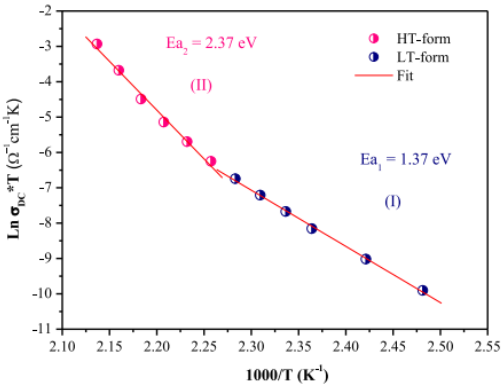

Fig. 12. Ln (σ_{DC}.T) versus reciprocal temperature of $[(C_2H_5)_4N]_2ZnI_4$ compound.

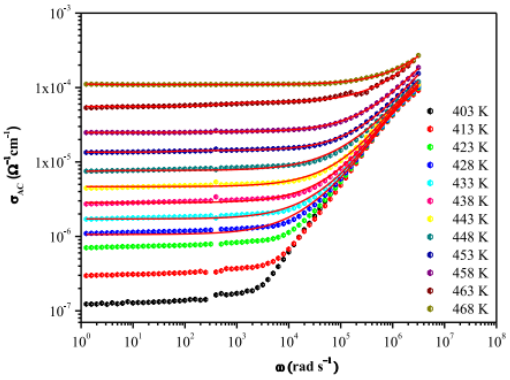

Fig. 13. AC conductivity *vs* frequency at several temperatures.

distinct regions, below (region I) and above (region II) the structural phase transition at 444 ± (5) K. As the temperature increases, the exponent S increases in the non-overlapping small polaron tunneling (NSPT) model whereas S decreases in the correlated barrier hopping (CBH) model [63,64]. From Fig. 14, we can conclude that, NSPT and CBH models able to describe the mobility of charge carrier in $[(C_2H_5)_4N]_2ZnI_4$ within the region I and II, respectively.

4-Conclusion

The $[(C_2H_5)_4N]_2ZnI_4$ organic-inorganic compound was synthesized by slow evaporation at room temperature. The structure of tetragonal in symmetry (space group $P\,\bar{4}\,2_1m$) is built up from $[ZnI_4]^{2-}$ anion surrounded by tetra-ethylammonium (TEA) cations. This semi-conducting compound has a 3.9 eV band gap which makes it interesting in solar cell domain. A reversible first order structural phase transition is detected at 444 K by differential thermal analyses (DTA) and by temperature-controlled X-ray powder diffraction. The changes in thermal expansion coefficients (TEC) along both the *a* and c axes at around 373 K is attributed to a phase transition of second-order caused by small displacements/reorientations of the $[(C_2H_5)_4N]^+$ cations in the crystal structure.The temperature dependence of DC conductivity and of the exponent S in the Jonscher's law clearly demonstrate that a change of

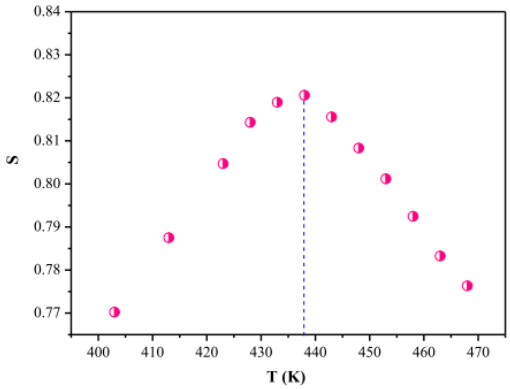

Fig. 14. Variation of S as a function of temperature for $[(C_2H_5)_4N]_2ZnI_4$.

conduction regime takes place at the first order phase transition at around 444 K. Below and above this temperature, NSPT and CBH models can describe the mobility of charge carriers in $[(C_2H_5)_4N]_2ZnI_4$.

CRediT authorship contribution statement

H. Elgahami: Writing – original draft. **J. Lhoste:** Writing – original draft. **S. Auguste:** Investigation, Software, Visualization. **G. Corbel:** Writing – original draft. **A. Oueslati:** Visualization, Validation, Writing – review & editing.

Declaration of competing interest

The authors declare that they have no known competing financial interests or personal relationships that could have appeared to influence the work reported in this paper.

References

[1] W. Trigui, A. Oueslati, F. Hlel, A. Bulou, J. Mol. Struct. 1106 (2016) 19.
[2] M. Era, S. Morimoto, T. Tsutsui, S. Saito, Appl. Phys. Lett. 65 (1994) 676.
[3] C.R. Kagan, D.B. Mitzi, C.D. Dimitrakopoulos, Science 286 (1999) 945.
[4] I. Chung, B. Lee, J. He, R.P.H. Chang, M.G. Kanatzidis, Nature 485 (2012) 486.
[5] M.L. Michael, J. Teuscher, T. Miyasaka, N.M. Takurou, H.J. Snaith, Science 338 (2012) 643.
[6] H.S. Kim, C.R. Lee, J.H. Im, K.B. Lee, T. Moehl, A. Marchioro, S.J. Moon, R. Humphry-Baker, J.H. Yum, J.E. Moser, M. Gratzel, N.G. Park, Sci. Rep. 2 (2012) 591.
[7] J. Burschka, N. Pellet, S.J. Moon, R. Humphry-Baker, P. Gao, M.K. Nazeeruddin, M. Gratzel, Nature 499 (2013) 316.
[8] H. Shimizu, N. Abe, N. Kokubo, N. Yasuda, S. Fujimoto, T. Yamaguchi, S. Sawada, Solid State Commun. 34363 (1980).
[9] A. Sawada, J. Sugiyama, M. Wada, Y. Ishibashi, J. Phys. Soc. Jpn. 48 (1980) 1773.
[10] K. Gesi, M. Iizumi, J. Phys. Soc. Jpn. 48 (1980) 1775.
[11] H. Mashiyama, S. Tanisaki, J. Phys. Soc. Jpn. 50 (1981) 1413.
[12] S. Sawada, Y. Shiroishi, A. Yamamoto, M. Takashige, M. Matsuo, J. Phys. Letters. A 67 (1978) 56.
[13] M. Wada, M. Suzuki, A. Sawada, Y. Ishibashi, K. Gesi, J. Phys. Soc. Jpn. 50 (1981) 1813.
[14] S. Sawada, Y. Shiroishi, A. Yamamoto, M. Takashige, M. Matsuo, J. Phys. Soc. Jpn. 44 (1978) 687.
[15] K. Gesi, R. Perret, J. Phys. Soc. Jpn. 57 (1988) 3698.
[16] G.D. Stucky, J.B. Folkers, T. Kistenmacher, Acta Crystallogr. 23 (1967) 1064.
[17] A. Mahoui, J. Lapasset, J. Moret, P. Saint-Grégoire, Z. für Kristallogr. - Cryst. Mater. 210 (1995) 125.
[18] I. Dakhlaoui, K. Karoui, F. Hajlaoui, N. Audebrand, T. Roisnel, J. Mol. Struct. 1231 (2021), 129684.
[19] T. Melia R. Merrifield, J. Chem. Soc. Inorg. Phys. Theor. (1970) 1166.
[20] T.P. Melia, R. Merrifield, J. Chem. Soc. Inorg. Phys. Theor. 19 (1971) 1258.
[21] N. Drissi, K. Karoui, F. Jomni, A. Ben Rhaiem, J. Phys. 83 (2016) 349.
[22] C.P. Landee, E.F. Westrum, J. Chem. Thermodyn. 11 (1979) 247.
[23] M. Iwata, Y. Ishibashi, J. Phys. Soc. Jpn. 60 (1991) 3245.
[24] Z. Czapla, S. Dacko, Ferroelectrics 125 (1992) 17.
[25] W.T.A. Harrison, R.A. Howie, J. Skakle, J.L. Wardell, Acta Crystallogr. C56 (2000) e124.
[26] N. Mercier, N. Louvain, W.H. Bi, CrystEngComm 11 (2009) 720.
[27] G. Volonakis, M.R. Filip, A.A. Haghighirad, N. Sakai, B. Wenger, H.J. Snaith, F. Giustino, J. Phys. Chem. Lett. 7 (2016) 1254.
[28] W.T.A. Harrison, R.A. Howie, J. Skakle, J.L. Wardell, Acta Crystallogr. C 56 (2000) e124.
[29] G.M. Sheldrick, SADABS, Program for Empirical Absorption Correction of AreaDetector Data, University of Gottingen, Germany, 1996, p. 467.
[30] G.M. Sheldrick, SHELXL-97, vol. 112, Program of Crystal Structure Refinement University of Gottingen, 1997.
[31] L.J. Farrugia, WinGX suite for small-molecule single-crystal crystallography, Appl. Crystallogr. 32 (1999) 837.
[32] A. Le Bail, H. Duroy, J.L. Fourquet, Mater. Res. Bull. 23 (1988) 447.
[33] J. Rodríguez-Carvajal, J. Phys. B Condens. Matter 192 (1993) 55.
[34] J. Zaleski, R. Jakubas, Z. Galewski, L. Sobczyk, Z. Naturforsch. 44 (1989) 1102.
[35] G. Helgesson, S. Jagner, G. Vicentini, C. Rodellas, L. Niinistö, ActaChemicaScandinavica 41a (1987) 556.
[36] D.S. Brown, F.W.B. Einstein, D.G. Tuck, Inorg. Chem. 8 (1969) 14.
[37] G.D. Stucky, J.B. Folkers, T.J. Kistenmacher, Acta Crystallogr. 23 (1967) 1064.
[38] B.S. Kirsh, *The Technocrates, Prophets Of Automation*, by Henry Elsner, Jr vol. 22, Syracuse University Press, Syracuse, New York, 1967, p. 589, 1967, $10,00,Relations industrielles.
[39] A. Mahoui, J. Lapasset, J. Moret, P. Saint Grégoire, Acta Crystallogr. C 52 (1996) 2671.
[40] M. Kahrizi, M.O. Steinitz, Solid State Commun. 70 (1989) 599.
[41] A.J. Wolthuis, W.J. Huiskamp, L.J. de Jongh, R.L. Carlin, Physica B 142 (1986) 301.

[42] A. Mahoui, J. Lapasset, J. Moret, J. Acta Crystallogr. C 50 (1994) 358.
[43] R.D. Russel, P.A. Tucker, Whittaker, Acta Crystallogr. B 31 (1975) 2530.
[44] N. Mahfoudh, K. Karoui, K. Khirouni, A. Ben Rhaiem, J. Phys. B Condens. Matter 554 (2019) 126.
[45] I.B.H. Sadok, F. Hajlaoui, K. Karoui, N. Audebrand, Th. Roisnel, N. Zouari, J. Phys. Chem. Solid. 129 (2019) 71.
[46] C. Ben Mohamed, K. Karoui, M. Tabellout, A. Ben Rhaiem, J. Alloys Compd. 688 (2016) 407.
[47] F. Yakuphanoglu, J. Alloys Compd. 507 (2010) 184.
[48] J.W. Gooch, Kubelka-Munk Equation, Encycl. Dict. Polym. 414 (2011).
[49] S. Kalyanaraman, P.M. Shajinshinu, S. Vijayalakshmi, J. Phys. B Condens. Matter 482 (2016) 38.
[50] J. Cimanowski, J. Acta Agrobot. 22 (2015) 265.
[51] C. Ben Mohamed, K. Karoui, A. Ben Rhaiem, J. Phase Transitions 91 (2018) 1162.
[52] H. Kchaou, K. Karoui, K. Khirouni, A. Ben Rhaiem, J. Alloys Compd. 728 (2017) 936.
[53] K. Karoui, A. Ben Rhaiem, F. Hlel, M. Arous, K. Guidara, J. Mater. Chem. Phys. 133 (2012) 1.
[54] M. Ben Gzaiel, A. Oueslati, F. Hlel, M. Gargouri, Phys. E Low-dimens. Syst. Nanostruct. 83 (2016) 405.
[55] H. Nefzi, F. Sediri, H. Hamzaoui, N. Gharbi, Mater. Res. Bull. 48 (2013) 1978.
[56] S. Jayaseelan, P. Muralidharan, M. Venkateswarlu, N. Satyanarayana, Mater. Sci. Eng., B 119 (2005) 136.
[57] M. Ram, Solid State Sci. 12 (2010) 350.
[58] K.S. Rao, P.M. Krishna, D.M. Prasad, J.-H. Lee, J.-S. Kim, J. Alloy and Compd. 464 (2008) 497.
[59] A.K. Jonscher, Nature 276 (1977) 673.
[60] R. Cheruku, Li Vijayan, G. Govindaraj, Mater. Sci. Eng., B 177 (2012) 771.
[61] H. Elgahami, M. Ajili, T. Roisnel, A. Oueslati, J. Solid State Chem. 311 (2022), 123108.
[62] E.M. El-Menyawy, I.T. Zedan, A.M. Mansour, H.H. Nawar, J. Alloy and Compd. 611 (2014) 50.
[63] A. Ghosh, Phys. Rev. B 42 (1990) 5665.
[64] H. Hassib, A. Abdel Razik, Solid State Commun. 147 (2008) 345.